
High-Spatial-Resolution Studies of UV-Laser-Damage Morphology in SiO₂ Thin Films with Artificial Defects

Introduction

The importance of conducting a quantitative, high-spatial-resolution investigation of thin-film-damage morphology is twofold. First, comparison of spatial frequencies of the damaged site with the surrounding unmodified material may indicate the presence of particular processes in the damage event. For instance, a smooth surface that is missing granular film structure usually points to melting of thin-film material. Second, experimental data on geometry (lateral size, depth, cross-sectional profiles, volume) of the modified material provide vital information for theoretical-model validation.

High-resolution studies of laser damage in thin films have generated a significant amount of information regarding morphological changes in coating materials under different conditions (wavelength and pulse length, fluence, spot size) of irradiation. The application of high-resolution methods established that nanosecond-pulse-driven damage in thin-film coatings is linked to localized absorbing defects. For lasers operating in the UV spectral range, even a few nanometer-sized defects can initiate thin-film damage in the form of craters.¹

Despite this fact, very few systematic studies link thin-film-defect parameters and local laser fluence to micron- and nanometer-scale modification of thin-film material. The most important reason for that is that size and density of defects in laser-quality coatings are extremely small,¹ thus precluding any characterization. An investigation of the role of nodular defects in multilayer 1.06- μm laser damage^{2,3} serves as one example of such studies. To assuage this challenge, SiO₂ thin films with embedded gold nanoparticles serving as artificial absorbing defects have been explored⁴⁻¹³ and have proven to be a very useful model system for unraveling damage mechanisms.

Previous experiments with this system subjected to UV, nanosecond pulses showed that during the laser pulse, absorption is not confined to the absorbing defect.⁷ Upon defect-temperature rise, modification of the surrounding matrix takes place followed by effective growth of the absorbing volume.

According to theoretical predictions by M. Feit *et al.*,^{14,15} this growth saturates when reaching a scale of the order of the excitation wavelength λ . The same theory establishes scaling relations between damage-crater diameter and particle-lodging depth at fixed laser-fluence conditions.

A detailed theoretical description of the laser-pulse-energy deposition followed by crater formation remains a challenge even for this well-characterized model system. The initial stages, including kinetics of absorption and heating in the gold particle and energy transfer processes at the particle-matrix interface, were studied by P. Grua *et al.*^{16,17} It was shown that thermionic electron emission from gold inclusion is an important mechanism of energy transfer to the surrounding matrix.

Promising results have been obtained with the one-dimensional (1-D) hydrodynamic code DELPOR (F. Bonneau *et al.*¹⁸), including electromagnetic effects, thermal conduction, radiative transfer, ionization by thermal UV radiation, and propagation of shock waves. From this code, combined with the two-dimensional (2-D) hydrodynamic code HESIONE,¹⁹ which calculates mechanical effects using brittle-fracture models, a crater-formation picture emerges for relatively large, 600-nm particles in qualitative agreement with experiment.^{8,9} Remaining difficulties here are related to the paucity of accurate data on electrical, thermal, optical, and mechanical properties of materials in the solid, liquid, vapor, and plasma states in the temperature range from ambient to $\sim 10^4$ K.

In this work, we used 18.5-nm gold nanoparticles as artificial defects embedded in a SiO₂ thin film at several well-defined distances from the film surface. Atomic force microscopy (AFM) is used to investigate the damage morphology produced by 351-nm, 0.5-ns laser pulses and dominated by submicrometer-scale craters. Variation in crater diameter, depth, and shape with laser fluence and particle-lodging depth is systematically studied and compared with phenomenological-theory^{14,15} predictions. The contributions of two major mechanisms of damage crater formation—melting/evaporation and fracture/ejection—are evaluated.

Experimental

A SiO₂ thin-film sample containing gold nanoparticles is prepared in three steps: Initially, a 240-nm SiO₂ thin film is deposited by *e*-beam evaporation onto a cleaved fused-silica (Corning 7980, 14 × 6 × 5 mm) substrate. Next, gold nanoparticles of average diameter $d = 18.5$ nm (standard deviation = 0.9 nm; data from Ted Pella, Inc.) in the form of a gold colloid are diluted in isopropanol and deposited by a micropipette onto the SiO₂-coated surface. Finally, the sample is returned to the coating chamber and coated with an additional layer of SiO₂. Five samples are prepared as described above, all coated in the same deposition run, each with a different capping-layer thickness: 30 nm, 60 nm, 110 nm, 190 nm, and 240 nm. A more detailed description of the sample preparation can be found in Ref. 7.

An Nd-doped glass laser (frequency-tripled, 351-nm, 0.5-ns pulses; 400- μ m spot size) is used for sample irradiation. Laser-beam incidence on the entrance surface was slightly off-normal ($\sim 7^\circ$) in order to prevent influence of the back-reflection ($\sim 4\%$) from the sample exit surface. No damage is observed within the bulk or at the rear surface of the cleaved fused-silica substrate at the entrance-surface fluence < 8.1 J/cm². Laser-fluence profiles are obtained from images captured by a low-noise (few electrons/pixel/s at a temperature of -40°C), high-dynamic-range, charge-coupled-device (CCD) imaging camera (Spectral Instruments, Inc.) in a sample equivalent plane. Correlation between laser-spot intensity and areal density and average size of damage craters allows attributing the peak fluence to the damage center (see Fig. 101.20). Once it is

done, laser fluence versus sample-coordinate dependence can be easily established and damage crater geometry versus fluence behavior investigated. The particular laser fluence at which the crater diameter approaches zero value is defined as the nanoscale damage threshold.

The damage morphology investigation is conducted by means of atomic force microscopy (AFM) (NanoscopeIII, Digital Inst./Veeco) operated in tapping mode. High-aspect-ratio (better than 5:1) silicon probes are used to ensure convolution-free imaging of craters with steep wall angles approaching 80° with the horizon.

Results and Discussion

1. Damage Morphology

Submicrometer-sized craters, formed exclusively at nanoparticle locations,⁷ are the main damage-morphology features. In the case of shallow particle-lodging depths (30 nm and 60 nm) and close to the crater-formation threshold, the craters are very small, with a typical lateral size of 35 to 50 nm, and randomly shaped (see Fig. 101.21). The absence of a rim elevated above the average surface level and the random shape point to a material-removal mechanism without significant melting. The portion of the film above the particle is probably ejected under pressure created in the process of particle heating. This picture holds in the fairly narrow fluence range of 0.5 to 0.8 J/cm² for a 60-nm lodging depth, and in the range of 0.6 to 4 J/cm² for a 30-nm lodging depth [detailed in the **Crater Geometry Versus Laser-Fluence Behavior** section (p. 28)]. Beyond this initial fluence range, a crater takes a

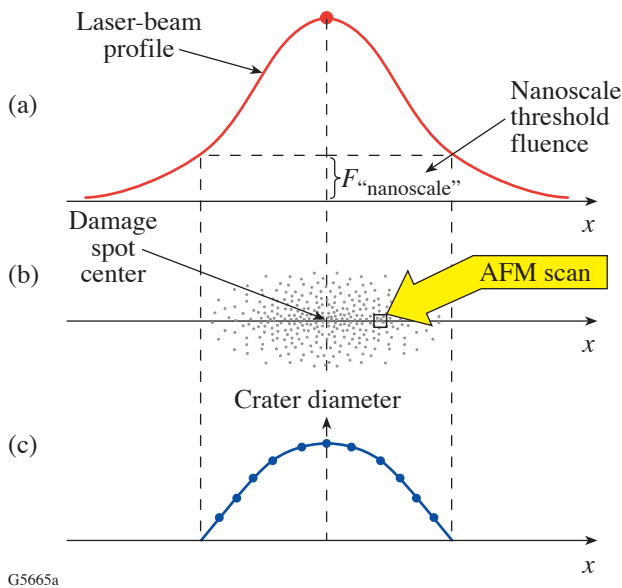


Figure 101.20

Experimental scheme of nanoscale damage threshold and crater diameter versus laser-fluence determination. (a) Laser-spot x -intensity profile; (b) damage crater areal distribution; (c) crater diameter versus x coordinate position. The nanoscale threshold value is defined as the laser fluence at which the crater diameter is approaching zero value.

conventional symmetric shape with an elevated rim, indicative of melting and resolidification (Fig. 101.22). The smooth internal surface of these craters, shown in Fig. 101.23, is missing the granular texture of the surrounding film, which is characteristic of melting and explosive vaporization. Later, this type of crater will be referred to as a *regular* crater. It is also

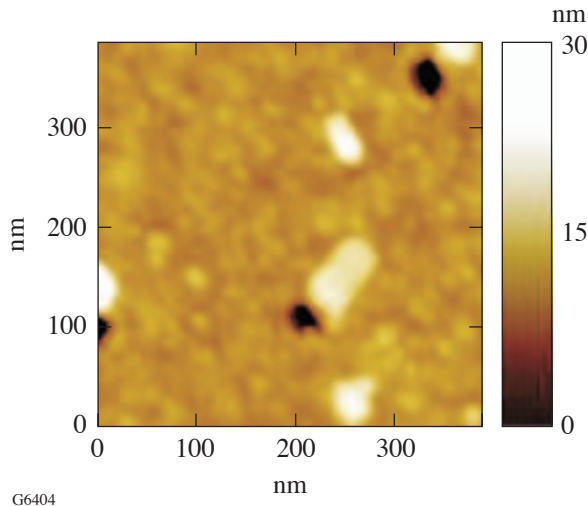


Figure 101.21
Craters originated by particles with 30-nm lodging depth at close-to-threshold conditions, $0.4\text{-}\mu\text{m} \times 0.4\text{-}\mu\text{m}$ AFM image.

useful to note here that under the term vaporization, we consider all processes transforming material from the liquid phase into the vapor phase, including fragmentation (nanocluster formation).

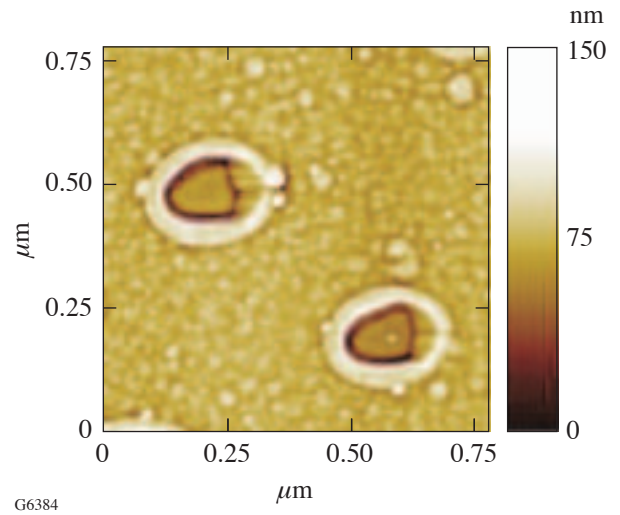


Figure 101.23
Internal walls of craters originated by particles with 60-nm lodging depth at fluences $F > 1 \text{ J/cm}^2$ are missing granular structure of the surrounding film, indicative of melting and vaporization. Contrast enhancement function is applied in order to amplify high spatial frequencies, $0.8\text{-}\mu\text{m} \times 0.8\text{-}\mu\text{m}$ AFM image.

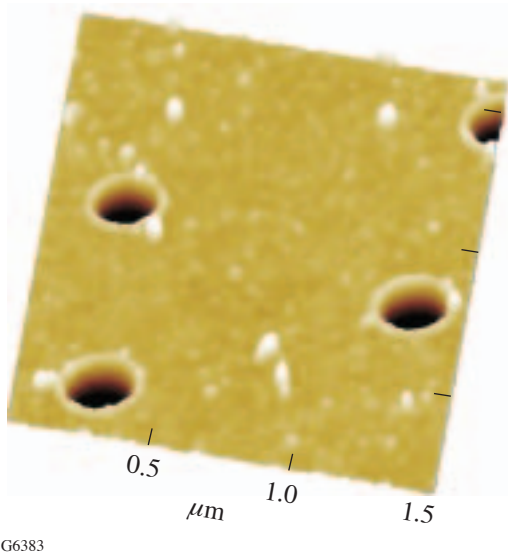


Figure 101.22
Typical craters originated by particles with 60-nm lodging depth at fluence $F = 6.2 \text{ J/cm}^2$, $1.5\text{-}\mu\text{m} \times 1.5\text{-}\mu\text{m}$ AFM scan.

Damage-crater morphology caused by particles at 190-nm and 240-nm lodging depths is very different. From this point this type of crater will be referred to as a *complex* crater. The lateral shape of these craters (depicted in Fig. 101.24) is asymmetric, most often with partial circularity and sharp corners — all pointing to hoop-stress-driven material removal. On the other hand, their internal surfaces are smooth (Fig. 101.25), indicative of the melting point having been reached. A cross-sectional profile of a typical complex crater is also depicted in Fig. 101.25. It clearly shows two parts: a narrow “channel” with vertical walls at the bottom and a wide upper part with inverse aspect ratio. Absence of the rim around the crater indicates that energy deposited in the upper part of the crater was insufficient to cause molten material flow at the outer crater boundary.

One possible scenario for the formation of this type of crater is as follows: Initially, absorption inside and around the particle causes melting and superheating of the material within the channel volume. This process is accompanied by rapid internal-pressure buildup and shock-wave generation. When the

generated hoop stress exceeds the strength of the silica material (fracture toughness $\sim 0.75 \text{ Mpa} \cdot \text{m}^{1/2}$ for bulk fused silica), fracture along the boundaries of the upper part of the crater takes place, followed by ejection of both the fractured portion and the molten material from within the channel.

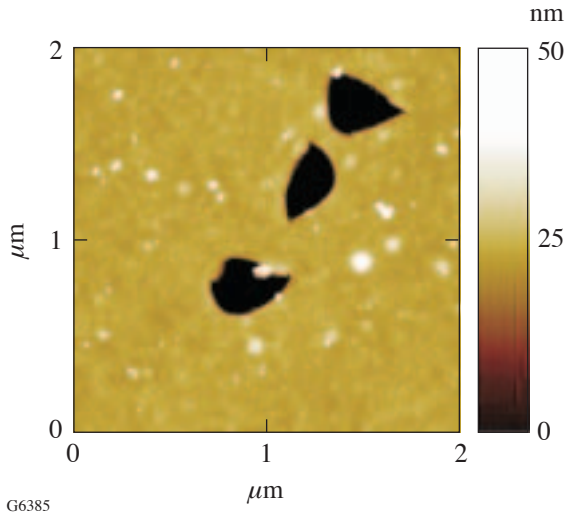


Figure 101.24
Craters originated by particles with 190-nm lodging depth. Random, partially circular shapes pointing to hoop-stress-driven material removal of the top film layer, 2- $\mu\text{m} \times 2\text{-}\mu\text{m}$ AFM scan.

Formation of such a complex crater was also reported in Refs. 9 and 10, where much larger gold particles of 600 nm were embedded in a SiO₂ film matrix. In the case of 110-nm lodging depth, both types of crater geometries characteristic for shallow and deep particle locations are present (Fig. 101.26).

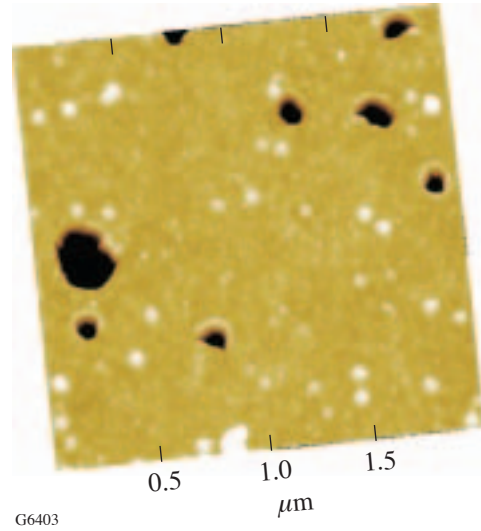


Figure 101.26
Craters formed from intermediate, 110-nm-deep particle location. Both types of craters, regular and complex, are generated simultaneously, 2- $\mu\text{m} \times 2\text{-}\mu\text{m}$ AFM scan.

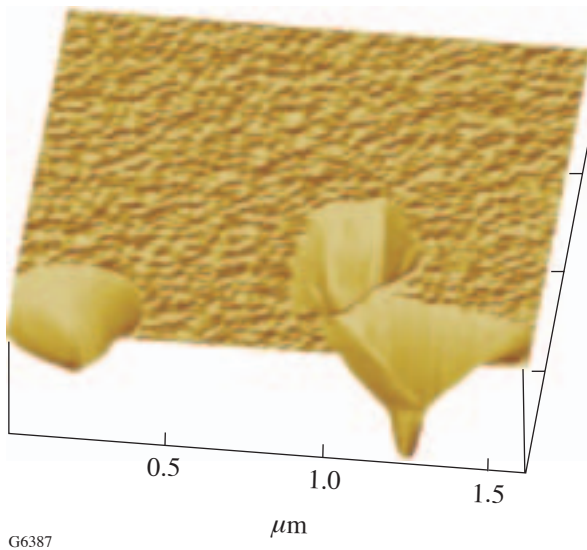


Figure 101.25
Smooth internal walls of complex craters point to the melting point having been reached. Cross-sectional crater profile reveals presence of two parts, a narrow channel on the bottom and a wide upper part removed by fracture.

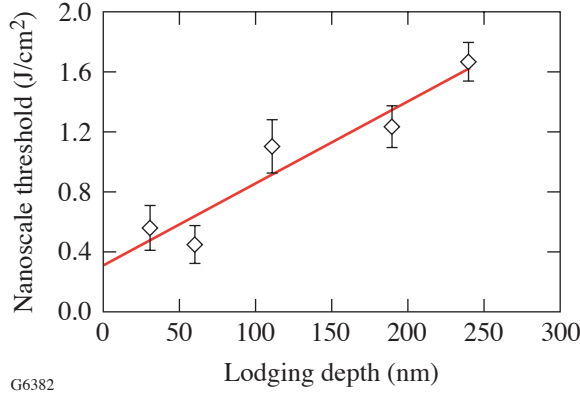
2. Nanoscale Damage Thresholds

The definition of damage threshold has always been linked to the method of detecting material modification. Consequently, type and sensitivity of the damage-detection equipment have a major impact on measured threshold values. The most commonly used optical methods are adequate for practical evaluation of optical-component survival in high-power laser systems or for studying particular trends, like pulse-length dependencies. Still, these methods are very difficult to use for meaningful comparison with the theories describing the dynamics of the damage process.

AFM investigation of crater size versus laser-fluence dependencies allows one to find the crater-formation threshold (nanoscale threshold) as that fluence at which the crater diameter approaches zero. It corresponds to a maximum fluence causing only limited localized melting without material removal. This definition is in much better agreement with theories that consider matrix melting as the onset of damage.

The results of nanoscale-threshold measurement summarized in Table 101.III and in Fig. 101.27 show a threshold

increase with increasing particle-lodging depth. An explanation comes from the fact that at near-threshold conditions, deeper particles consistently produce deeper and larger craters [see the **Crater Geometry Versus Laser-Fluence Behavior** section (p. 28)]. Consequently, larger material removal requires more energy to be absorbed for a crater to form.



G6382

Figure 101.27
Nanoscale damage thresholds as a function of particle-lodging depth.

Table 101.III: Nanoscale damage thresholds.

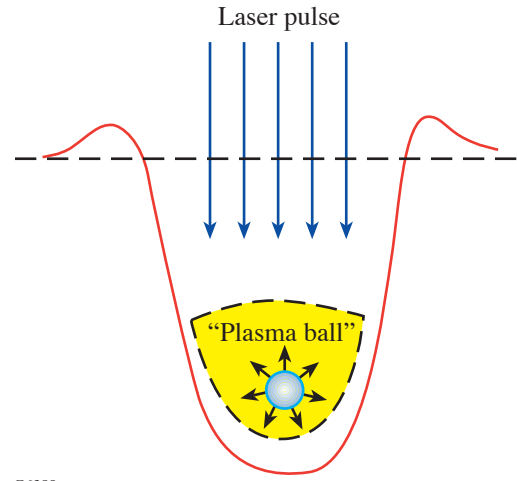
Particle Lodging Depth		Nanoscale Threshold (J/cm ²)
<i>h</i> ₀ ,nm	<i>h</i> ₀ / <i>d</i>	
30	1.6	0.56±0.15
60	3.2	0.45±0.10
110	5.9	1.11±0.21
190	10.3	1.24±0.16
240	13.0	1.67±0.14

3. Theoretical Approach to Crater Formation

As was mentioned above, numerical calculations of damage-crater-formation kinetics and final geometries are very challenging. In this work, we compare experimental results on crater lateral size behavior as a function of fluence and absorbing defect lodging depth with phenomenological-theory^{14,15} predictions.

The main assumptions and results of this theory can be formulated as follows: If the temperature around an absorbing defect exceeds a critical value, a thermal explosion²⁰ takes

place. In this process, the defect-surrounding matrix becomes absorptive and undergoes rapid heating and ionization with plasma density exceeding critical. This process is depicted schematically in Fig. 101.28.



G6389

Figure 101.28
Schematic of the plasma-ball formation around an absorbing defect.

Considering that the major part of the absorbed energy goes into ionization of the material, the ionized volume (plasma “fire ball”) radius *a* grows exponentially with laser fluence *F*:

$$a = a_0 \exp \gamma, \tag{1}$$

where the growth factor γ scales linearly with *F*.

At high laser fluences, growth of the plasma ball tends to saturate, and its diameter reaches a maximum value of the order of the absorbed-light wavelength λ . In this case absorbed energy can be estimated as

$$E = F\pi\lambda^2. \tag{2}$$

The radius *R* of a produced crater is determined by *E*, the energy deposited in the plasma-ball volume, and *h*, the lodging depth of the initiating absorber.

At fixed energy *E*, the crater radius as a function of lodging depth *h* is given by the expression

$$R^2 = h^{2/3} (h_d^{4/3} - h^{4/3}), \tag{3}$$

where h_d is the maximum lodging depth at which a crater is still formed. For this depth, energy E is the threshold energy for crater formation and corresponds to the *nanoscale damage threshold*.

The maximum crater radius R_m and corresponding lodging depth h_m are given by

$$R_m = \sqrt{2}h_m \approx 0.6h_d \text{ and } h_m \approx 0.44h_d. \quad (4)$$

At high laser fluences, when the growth of the plasma ball saturates, crater radius growth with fluence can be approximated by 1/3 power law:

$$R \sim F^{1/3}. \quad (5)$$

4. Crater Geometry Versus Laser-Fluence Behavior

a. Crater-diameter variation with fluence. Geometrical parameters measured for the two types of crater morphology are schematically presented in Fig. 101.29. Henceforth, a cross-sectional profile similar to Fig. 101.29(a) will be referred to as a regular crater, and one similar to Fig. 101.29(b) as a complex crater.

Crater diameter D is measured by means of the cross-sectional analysis of AFM images as crater opening at average surface level (see Fig. 101.29). In the case of asymmetric craters, diameter values are taken as an average of measurements taken in two orthogonal directions crossing the center of gravity of the crater opening area. Each data point in the $D(F)$

graph is obtained as an average for all craters (2 to 10) imaged within a particular AFM scan ($2 \mu\text{m} \times 2 \mu\text{m}$ or $3 \mu\text{m} \times 3 \mu\text{m}$) and correlated with one fluence value.

This averaging allows variations to be smoothed out in the crater geometry for individual particle locations caused by the inhomogeneous thin-film environment. As shown earlier (see Ref. 7), variations in the particle/thin-film interface geometry strongly affect both absorption by the particle and energy transfer to the surrounding-film matrix. This effect is more pronounced at close-to-threshold conditions, when only particles with the best contact with the matrix are producing craters. At laser fluences many times exceeding threshold, the probability of crater formation is approaching 100% and, for regular craters, variation in crater size is significantly reduced.

Crater diameter versus fluence dependence for shallow lodging depths—30 nm and 60 nm—is presented in Fig. 101.30. In the case of the 60-nm lodging depth, it can be well approximated by a linear fit. More complex behavior is observed in the 30-nm case where, after a threshold jump, stagnation of diameter growth is measured in the fluence range of 0.6 to 4 J/cm². At higher fluences, almost exponential growth sets in, and at $F > 7 \text{ J/cm}^2$, 30-nm and 60-nm curves tend to merge together.

An explanation for this behavior in the case of 30-nm lodging depth may be found in the coating geometry (see Fig. 101.31). The coating above the particle is growing like a nodule and forms a spherical bump with lateral size L for which AFM measurement (unirradiated site) gave an average value of 47 nm. This value fits well within crater diameter sizes of 35 to 50 nm measured in the fluence range of 0.6 to 4 J/cm². Together with the typical crater depth of ~30 nm this points to material removal within one nodular volume, indicated by the dashed line in Fig. 101.31. Shallow particle location and gold-silica thermal mismatch imply reduced strength of the coating within the nodular volume described above and lend support for the following explanation: Upon energy absorption from the laser pulse and particle heating, pressure applied to the portion of the coating above the particle may suffice for its ejection without melting of the surrounding matrix. With an increase in laser fluence, increased pressure leads to even faster ejection and, possibly, additional heating of the removed material, but still without reaching a critical temperature at the particle/matrix interface. Eventually, at a high-enough fluence ($>4 \text{ J/cm}^2$), coupling to the surrounding matrix takes place before material ejection, leading to dramatic growth in crater size. In the case of 60-nm lodging, a similar

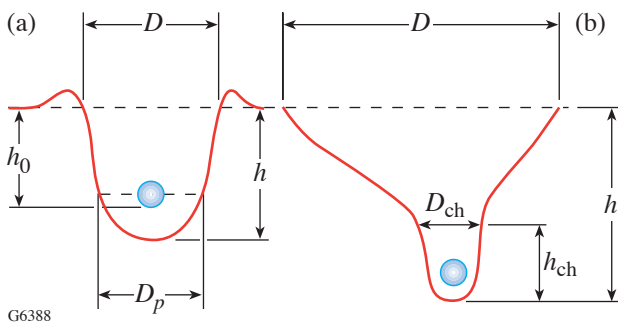
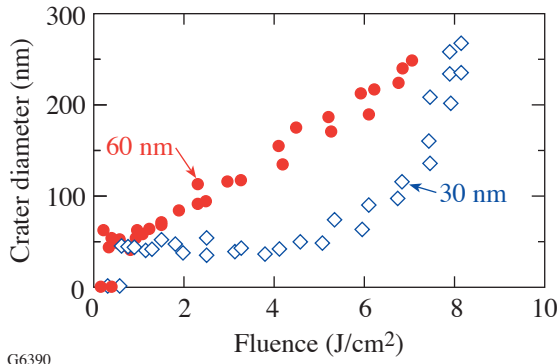


Figure 101.29

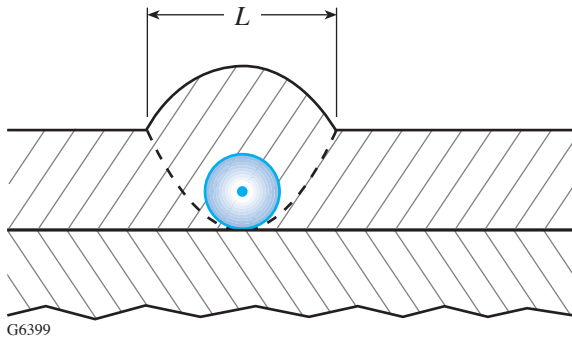
Cross-sectional profiles (not to scale) of (a) a regular crater and (b) a complex crater. Crater parameters measured by AFM: crater diameter D , crater depth h , crater channel diameter D_{ch} , channel depth h_{ch} , and crater width at particle-center position D_p .

stagnation range exists, though over a very narrow fluence range of 0.5 to 0.8 J/cm^2 . As one can notice, crater-diameter growth with fluence in the cases of 30-nm and 60-nm lodging (see Fig. 101.30) is much faster than $F^{1/3}$. This indicates that the plasma-ball saturation regime [see the **Theoretical Approach to Crater Formation** section (p. 27)] is not reached at fluences $< 8.1 \text{ J}/\text{cm}^2$.



G6390

Figure 101.30
Crater diameter versus fluence dependence for shallow particle-lodging depths, 30 nm and 60 nm.

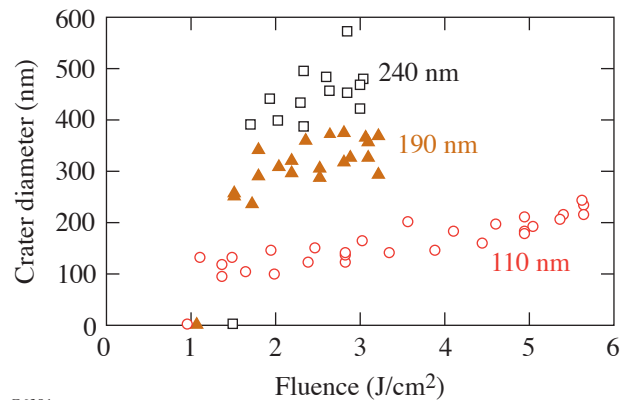


G6399

Figure 101.31
Thin-film geometry in case of 30-nm particle-lodging depth.

Crater diameter versus fluence dependence for 110-nm, 190-nm, and 240-nm lodging depths is depicted in Fig. 101.32, showing several features different from the case of shallow-lodging depth. The most notable difference is size. For instance, *at near-threshold conditions*, craters start with ~ 390 -nm diameter for 240-nm lodging compared to ~ 35 -nm diameter for 30-nm lodging. The reason goes beyond the trivial fact that at fluences just above threshold, deeper absorbers produce larger craters. More importantly, *different crater-formation*

processes come into play with increasing lodging depth. Regular craters [Fig. 101.29(a)] originate from shallow locations and are formed through the processes of melting and vaporization. Complex craters [Fig. 101.29(b)] originate from deep locations and, in addition to melting and vaporization of the material in the channel volume, have a significant amount of the top part of the material removed through a *fracture mechanism*. The process of material removal through fracture is much more favorable energetically than volumetric vaporization. In the former case, energy goes to molecular bond breaking in molecules associated only with a new surface compared to breaking bonds in the whole removed volume in the latter case. Even in the case when material removal proceeds through fragmentation (nanocluster formation), this picture holds.



G6391

Figure 101.32
Crater diameter versus fluence dependence for 110-nm, 190-nm, and 240-nm lodging depths.

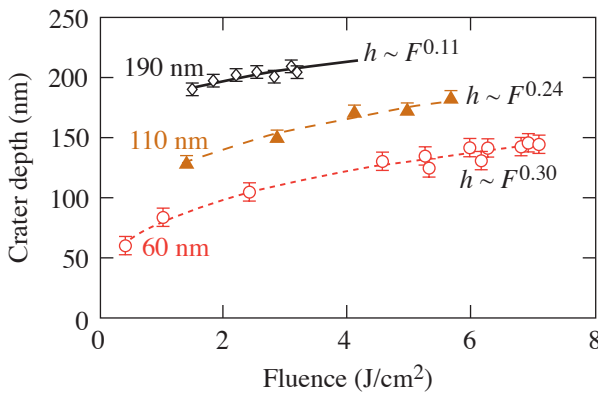
The growth of the crater diameter with fluence shows a lower growth rate for deep lodging depths, especially 190-nm and 240-nm lodgings. It can be understood considering the change in volume removed for each increment in crater diameter. At equal laser fluences, the same partial increment in the diameter will result in much larger volume removal for a large crater than for a small one. Consequently, it results in a larger fluence increment required for diameter increase and slower growth rate with fluence for larger craters.

The other feature in the $D(F)$ dependence for craters originating from deep (190-nm and 240-nm) particle locations (see Fig. 101.32) is a large variation in diameter. As was discussed earlier [see the **Damage Morphology** section (p. 24)], these craters are formed in a process involving fracture and ejection of the top portion of the coating. Due to the inhomogeneity of

the thin-film material, variation in local material strength and stress factors can significantly affect size and shape of the fracture-removed portion of the complex crater.

b. Crater-depth variation with fluence. Crater depth versus fluence behavior for 60-nm, 110-nm, and 190-nm lodging depths is presented in Fig. 101.33. At laser fluences slightly above threshold, crater-depth values are very close to the particle-lodging-depth values and deeper absorbers produce not only wider [see the **Crater-Diameter Variation with Fluence** section (p.28)] but also deeper craters. With fluence increase, however, the rate of depth growth with fluence is reduced with increasing lodging depth, which is clearly seen from power-law approximation of the $h(F)$ curves in Fig. 101.33. The explanation here is similar to the case of the $D(F)$ dependencies. Since crater volume is roughly proportional to h^3 , deep craters require a larger fluence increment to achieve the same partial depth increment compared to shallow craters.

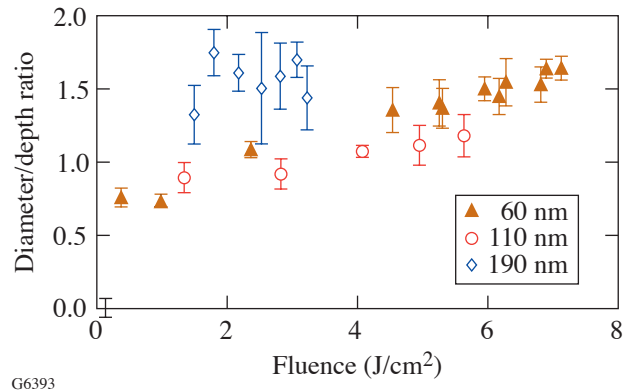
In the case of deep lodging depth (190 nm), the $h(F)$ dependence is much more deterministic than the $D(F)$ dependence, which is probably associated with the mechanism of complex-crater channel formation. The channel morphology suggests a channel-formation process very similar to the regular-crater formation involving phases of plasma-ball growth, melting, and vaporization. Comparison of channel geometry with regular crater geometry [see the **Features of Complex-Crater Channel Formation** section (p. 31)] lends strong support to this hypothesis.



G6392
Figure 101.33
Crater depth versus fluence dependence for 60-nm, 110-nm, and 190-nm lodging depths.

c. Transformation of crater aspect ratio with fluence. One of the important features of crater growth with laser fluence is the modification in aspect ratio. Changes in aspect ratio are linked to the kinetics of energy deposition and dissipation processes.

Figure 101.34 depicts crater diameter/depth ratio versus fluence for 60-nm, 110-nm, and 190-nm lodging depths. In the case of 60-nm and 110-nm lodging depths, there is clear evidence that the crater diameter grows faster than the depth, indicating that crater growth preferentially happens in the lateral dimension. For 190-nm lodging depth, large scatter in data points and a relatively narrow fluence range prevent a definitive conclusion. This trend is highlighted further by Fig. 101.35, which shows cross-sectional AFM profiles for three craters generated from the 60-nm lodging depth at three different fluences: 1 J/cm², 2.4 J/cm², and 6 J/cm². Comparison of diameter ratios to depth ratios underscores the dominance of the lateral scale in crater growth: $D_3/D_1 = 3.5$ and $h_3/h_1 = 1.7$.



G6393
Figure 101.34
Crater-diameter to crater-depth ratio as a function of fluence for 60-nm, 110-nm, and 190-nm lodging depths.

An interesting observation is that the D/h aspect ratio grows faster for more-shallow 60-nm lodging compared to 110-nm lodging. A probable explanation may be linked to the fact that instantaneous temperature distribution in the material depends on the absorber lodging depth. For a shallow initiation point, the proximity of the adiabatic boundary (silica/air interface) means that heat propagating from the absorbing volume (plasma ball) will be caught at the boundary and eventually spread laterally. Since plasma-ball growth preferentially proceeds toward the adiabatic boundary due to irradiation geometry and screening effect (see Fig. 101.28), fluence

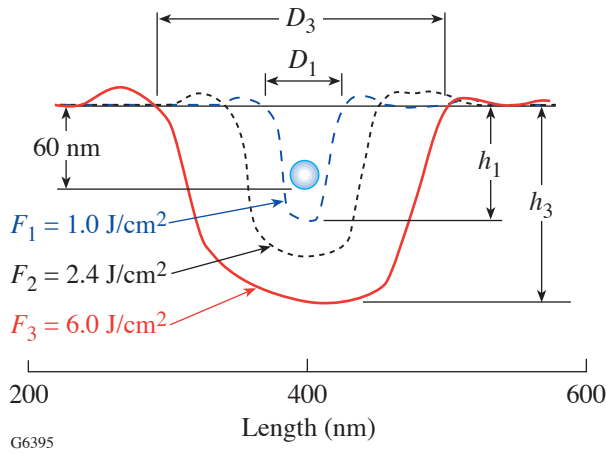


Figure 101.35
AFM-measured cross-sectional profiles for craters originated by particles with 60-nm lodging depth at fluences of 1.0 J/cm², 2.4 J/cm², and 6.0 J/cm². Crater growth with fluence is dominated by lateral scale.

increase should enhance lateral heat redistribution. For deep absorbers this effect may be less pronounced due to a more symmetric heat dissipation.

d. Features of complex-crater channel formation. To understand the mechanism of complex-crater formation, both channel diameter D_{ch} and depth h_{ch} [Fig. 101.29(b)] are measured as functions of fluence for 190-nm lodging. The results are plotted in Fig. 101.36 together with diameter and depth data (Figs. 101.30 and 101.33) for regular craters initiated by absorbers with 60-nm lodging. The striking agreement is seen for both diameter [Fig. 101.36(a)] and depth [Fig. 101.36(b)] values: channel data overlap well with regular-crater curves. This result lends support to a channel-formation mechanism through similar processes of melting and vaporization as in regular-crater formation. It also indicates that a *major part of the energy deposition in a complex crater takes place in the channel volume and goes into channel formation*. This immediately brings up a question about mechanism of the fracture generation leading to the removal of the complex crater’s upper part. The most probable candidate here is a shock wave generated during localized heating by a 0.5-ns laser pulse.

It is also useful to compare channel dynamics with the dynamics of the whole complex crater. For this purpose, D_{ch} and h_{ch} are normalized to their counterparts of the whole crater and plotted as a function of fluence in Fig. 101.37. Both dependencies show growth, which provides circumstantial evidence that plasma-ball and melt-front-propagation velocity

in the channel exceeds the fracture velocity in the studied range of fluence.

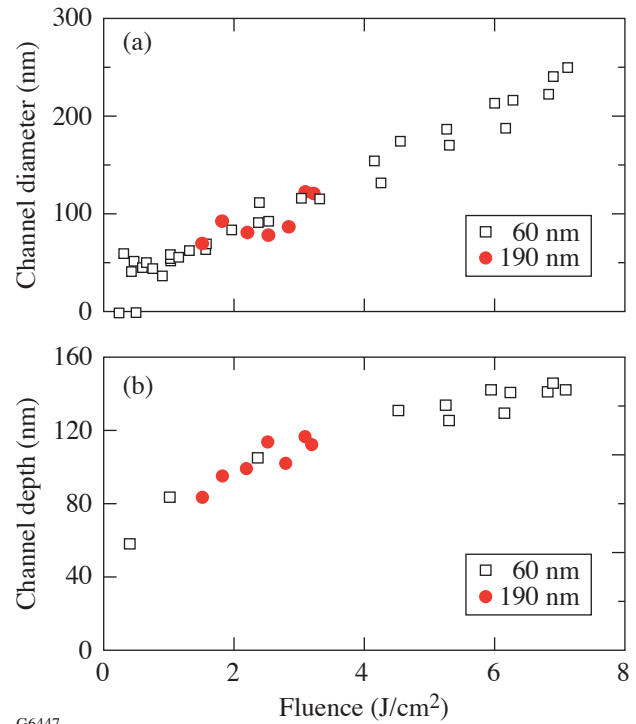


Figure 101.36
Complex-crater-channel diameter and depth variation with laser fluence: (a) channel diameter and (b) channel depth. Data for craters initiated by particles with 190-nm lodging depth are interleaved with data for regular craters originated by particles with 60-nm-deep location (see Figs. 101.30 and 101.33).

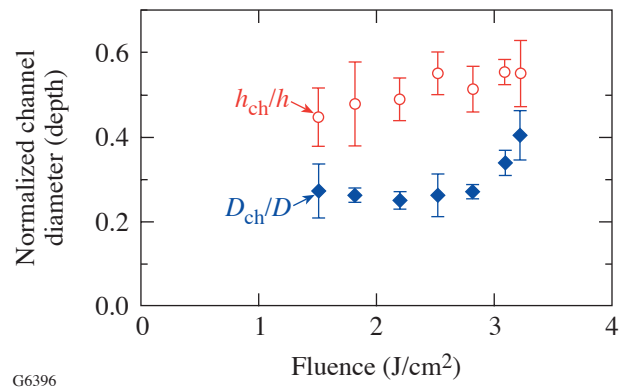
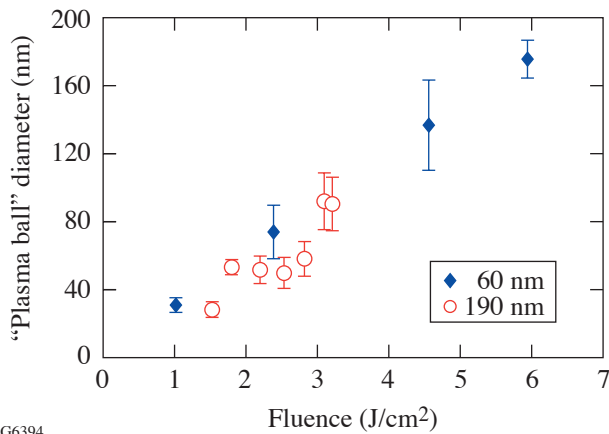


Figure 101.37
Channel diameter/crater diameter and channel depth/crater depth ratios as functions of fluence.

5. Estimates of Plasma-Ball Scale

Estimating the size of the plasma ball using only AFM data on crater geometry is not a straightforward task. Due to the dynamic nature of crater formation, the final shape of the regular crater is the result of interplay between processes of energy deposition, dissipation, hydrodynamic motion, and evaporation of the material. From this point of view, crater width at the particle-center position (see Fig. 101.28) is only remotely connected to the plasma-ball diameter. Nevertheless, with an increase in fluence and plasma-ball growth, part of the deposited energy used for crater formation will also grow due to the reduced role of dissipation processes (surface-to-volume ratio). It allows the use of crater width at the particle-center position D_p in the upper limit of fluence range as an estimate for the plasma-ball size. D_p values for 60-nm and 190-nm lodging are depicted in Fig. 101.38 as a function of fluence. In the case of 60-nm lodging, D_p shows linear growth and reaches a maximum value of ~ 180 nm at a fluence of ~ 6 J/cm² (~ 13 times threshold). According to phenomenological theory [see the **Theoretical Approach to Crater Formation** section (p. 27)], plasma-ball growth saturates upon reaching a size comparable with laser wavelength in SiO₂ film, $\lambda_f = 351/n_f \sim 250$ nm (n_f , film refractive index ≈ 1.4). Both the maximum measured value of $D_p \sim 180$ nm $\approx 3/4\lambda_f$ and the linear behavior of $D_p(F)$ suggest that plasma-ball growth is not reaching its saturation regime within the investigated fluence range.



G6394

Figure 101.38

Estimate of plasma-ball size. Crater width at the particle-center position taken as a function of fluence for the particle-lodging depths of 60 nm and 190 nm.

6. Scaling Relations

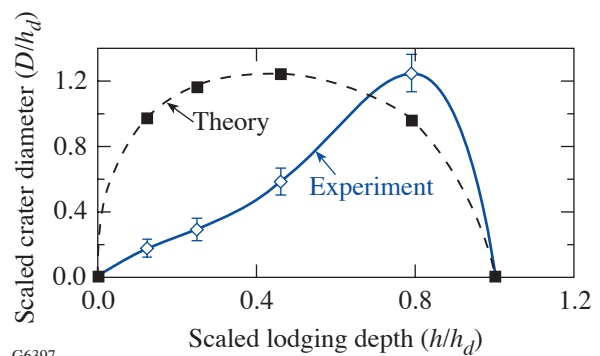
There are two lodging-depth cases where the crater is not formed: the first case is where the lodging depth is so large that the pulse energy deposited in the material is not enough to create a crater; the second case is zero depth, where the defect

can experience desorption without any modification of the film. At all intermediate locations, craters can be formed and the theory predicts a “bell”-shaped curve for crater diameter versus lodging depth dependence, in agreement with Eq. (3).

Our previous attempt to check scaling relations¹¹ with 8.4-nm particles showed qualitative agreement with theory, although only three relatively shallow lodging depths (10 nm, 30 nm, and 48 nm) were available at the time.

In this work, crater diameter was measured as a function of lodging depth at a fixed laser fluence of 1.67 J/cm²—the threshold fluence for the deepest lodging depth $h_d = 240$ nm. The results, normalized to h_d , are presented in Fig. 101.39 together with the theoretical curve predicted by Eq. (3). The departure from the theoretically predicted (“bell”-shaped) curve and shift in the peak position may be directly attributed to the change in the crater-formation mechanism with increasing lodging depth. The experimental curve shows clearly a transition taking place between 60-nm and 110-nm lodging depths and manifests the onset of the fracture-driven material removal. Significant change (4.3 times) in the diameter size for 190-nm lodging ($h/h_d = 0.79$) compared to 60-nm lodging ($h/h_d = 0.25$) points to the energetic preference of the fracture mechanism compared to melting and vaporization.

Figure 101.39 also shows surprisingly close agreement between the experimental maximum value of normalized crater size $D/h_d = 1.25$ and the theoretically predicted ≈ 1.2 value [see Fig. 101.39 and Eq. (4)]. Further investigations of scaling relations, preferably with only one dominating mechanism of crater formation, should test the strength of this result.



G6397

Figure 101.39

Scaled crater diameter versus scaled particle-lodging depth. Experimental data are taken at fluence 1.67 J/cm², corresponding to the crater-formation threshold for lodging depth $h_d = 240$ nm.

Conclusions

1. High-resolution investigation of 351-nm damage morphology in SiO₂ thin films with 18.5-nm gold nanoparticles serving as artificial, absorbing defects revealed sub-micrometer-scale craters as the main damage features.
2. Two different crater geometries are attributed to either (1) shallow absorbers and a melting/vaporization mechanism of crater formation, or (2) deep absorbers and complex-crater formation involving a combination of melting/vaporization and fracture.
3. The nanoscale thresholds (crater formation thresholds) increase with increasing particle-lodging depth, owing to the increased amount of energy required for craters to form.
4. At near-threshold conditions, craters initiated by deep absorbers are much larger than craters initiated from shallow depth mainly due to additional fracture-driven material removal from the top film layer. This mechanism is energetically much more efficient than melting and vaporization.
5. The growth of crater diameter and crater depth with laser fluence shows a higher rate for shallow absorbers compared to deep absorbers, which is explained by the difference in energy to be deposited to achieve the same partial increment in size.
6. Comparison with theoretical predictions for regular crater growth with fluence leads to the conclusion that the *saturation regime associated with the 1/3 power law is not reached* in the fluence range $<8.1 \text{ J/cm}^2$. This conclusion is strongly supported by a plasma-ball-size estimate showing linear growth with fluence and reaching a value of $\sim 3/4$ of a wavelength for 60-nm lodging depth and an $\sim 6\text{-J/cm}^2$ fluence.
7. Analysis of crater-aspect-ratio variation with laser fluence proved that *crater growth with fluence is dominant in the lateral dimension*, especially in the case of shallow absorbers.
8. Investigation of complex-crater formation showed that the channel part of the crater is formed through melting and vaporization with geometry and size closely resembling a regular crater, provided fluence is the same. The rate of channel scale growth with fluence is exceeding the rate of growth of the complex crater as a whole, indicating that the major part of energy deposition takes place in the channel volume.
9. Scaling relations between crater diameter and absorber lodging depth are influenced by changes in crater-formation mechanism with increasing lodging depth. Good agreement with theoretical predictions is found for scaled maximum-diameter values. Further understanding of the crater-formation picture can be achieved with the help of numerical modeling (as reported in Refs. 18 and 19) with realistic temperature-dependent material parameters and absorbing-particle sizes.

ACKNOWLEDGMENT

The authors would like to thank P. A. Jaanimagi, R. Boni, and M. Millecchia for help with implementation of the CCD imaging system. This work was supported by the U.S. Department of Energy Office of Inertial Confinement Fusion under Cooperative Agreement No. DE-FC52-92SF19460, the University of Rochester, and the New York State Energy Research and Development Authority. The support of DOE does not constitute an endorsement by DOE of the views expressed in this article.

REFERENCES

1. S. Papernov and A. W. Schmid, *J. Appl. Phys.* **82**, 5422 (1997).
2. M. C. Staggs *et al.*, in *Laser-Induced Damage in Optical Materials: 1991*, edited by H. E. Bennett *et al.* (SPIE, Bellingham, WA, 1992), Vol. 1624, pp. 375–385.
3. R. J. Tench, R. Chow, and M. R. Kozlowski, in *Laser-Induced Damage in Optical Materials: 1993*, edited by H. E. Bennett *et al.* (SPIE, Bellingham, WA, 1994), Vol. 2114, pp. 415–425.
4. S. Papernov, A. W. Schmid, R. Krishnan, and L. Tsybeskov, in *Laser-Induced Damage in Optical Materials: 2000*, edited by G. J. Exarhos *et al.* (SPIE, Bellingham, WA, 2001), Vol. 4347, pp. 146–154.
5. S. Papernov, A. W. Schmid, A. L. Rigatti, and J. D. Howe, in *Laser-Induced Damage in Optical Materials: 2001*, edited by G. J. Exarhos *et al.* (SPIE, Bellingham, WA, 2002), Vol. 4679, pp. 282–292.
6. A. V. Hamza *et al.*, in *Laser-Induced Damage in Optical Materials: 2001*, edited by G. J. Exarhos *et al.* (SPIE, Bellingham, WA, 2002), Vol. 4679, pp. 96–107.
7. S. Papernov and A. W. Schmid, *J. Appl. Phys.* **92**, 5720 (2002).
8. F. Bonneau *et al.*, *Appl. Phys. B* **75**, 803 (2002).
9. H. Bercegol *et al.*, in *Laser-Induced Damage in Optical Materials: 2002*, edited by G. J. Exarhos *et al.* (SPIE, Bellingham, WA, 2003), Vol. 4932, pp. 297–308.
10. H. Bercegol *et al.*, in *High-Power Laser Ablation IV*, edited by C. R. Phipps (SPIE, Bellingham, WA, 2002), Vol. 4760, pp. 1055–1066.
11. S. Papernov and A. W. Schmid, in *Laser-Induced Damage in Optical Materials: 2002*, edited by G. J. Exarhos *et al.* (SPIE, Bellingham, WA, 2003), Vol. 4932, pp. 66–74.
12. F. Bonneau *et al.*, *Appl. Phys. Lett.* **83**, 3855 (2003).

13. A. During *et al.*, in *Laser-Induced Damage in Optical Materials: 2003*, edited by G. J. Exarhos *et al.*, (SPIE, Bellingham, WA, 2004), Vol. 5273, pp. 366–372.
14. M. D. Feit *et al.*, in *Laser-Induced Damage in Optical Materials: 1997*, edited by G. J. Exarhos *et al.* (SPIE, Bellingham, WA, 1998), Vol. 3244, pp. 350–355.
15. M. D. Feit *et al.*, in *Laser-Induced Damage in Optical Materials: 2000*, edited by G. J. Exarhos *et al.* (SPIE, Bellingham, WA, 2001), Vol. 4347, pp. 316–323.
16. P. Grua and H. Bercegol, in *Laser-Induced Damage in Optical Materials: 2000*, edited by G. J. Exarhos *et al.* (SPIE, Bellingham, WA, 2001), Vol. 4347, pp. 579–587.
17. P. Grua *et al.*, Phys. Rev. B **68**, 035424 (2003).
18. F. Bonneau *et al.*, in *Laser-Induced Damage in Optical Materials: 2000*, edited by G. J. Exarhos *et al.* (SPIE, Bellingham, WA, 2001), Vol. 4347, pp. 308–315.
19. F. Bonneau *et al.*, Appl. Phys. B **78**, 447 (2004).
20. Yu. K. Danileiko, A. A. Manenkov, and V. S. Nechitailo, Sov. J. Quantum Electron. **8**, 116 (1978).